Stanford Exploration Project, Report 115, May 22, 2004, pages 39–57

Aliasing in prestack wavefield continuation migration

Brad Artman, Jeff Shragge, and Biondo Biondi[1]

ABSTRACT

With the widespread adoption of wavefield continuation methods for prestack migration, the concept of operator aliasing warrants revisiting. While zero-offset migration is unaffected by spatial aliasing due to the migration operator, this is not the case for prestack migration. This problem arises in any situation where sources and receivers are not collocated at every sampling point. Once anti-aliasing criteria have been calculated, aliased energy may be prevented from entering the image space by using a source function of appropriate band-width, or band-limiting the energy of the contributing data. As shot-profile migration is the most accurate and expensive imaging algorithm, data axes are commonly subsampled to save cost. We analyse the costs and benefits of implementing anti-aliasing measures to remediate unequal sampling intervals. While some bandwidth of the output image is lost in this process, it will attend to aliasing problems that will be most apparent in the shallow overburden and steeply dipping reflectors. Despite the loss in resolution, any proposed method still enjoys better bandwidth than source-receiver migration with the same data.

INTRODUCTION

The potential for aliasing phenomena to be introduced into Kirchhoff migration images from unaliased data is well documented. However, common wisdom holds that wavefield continuation migration does not introduce aliasing artifacts into the image. This is strictly true only for zero-offset migration. Thus, with the increasing use of prestack wave equation migration, it is important to establish when and how aliasing artifacts are introduced into the image through the wavefield-continuation migration process.

Migration of seismic data may give rise to aliasing problems in four distinct situations. Two of these aliasing situations we consider to be well understood and have effective solutions. These are: 1) improper discretization of the wavefield recorded at the surface can lead to aliasing of the features in the raw data (i.e. poorly sampled hyperbolas), and 2) not establishing an image space with twice finer sampling to accomodate the sum of spatial frequencies due to the multiplication of the wavefields in the imaging condition. Proper planning and layout of the acquisition mitigate the first problem, while Zhang et al. (2003) points out that interpolation of source and receiver wavefields by a factor of two eliminates the aliasing from multiplication.

[1]**email:** brad@sep, jeff@sep, biondo@sep

For the duration of this discussion we will assume both of these issues have been effectively controlled.

This paper presents an evaluation of two additional aliasing situations that have yet to be examined by the geophysical community. First, and the focus of this presentation, aliasing phenomenon can arise during the adoption of a wavefield coordinate system on which both source and receiver wavefields can be propagated and combined to create the image. Zero-offset migration, by definition, has common source and receiver locations. However, prestack migration requires choosing from two probably unequal source and receiver sampling intervals (doubly compounded for 3D surveys). This paper explores the ramifications of this problem and defines appropriate bandlimits. Finally, the extrapolation operator can introduce aliasing by moving energy to too high wavenumbers as it convolves the wavefields with the earth velocity model. During later propagation steps, that same energy could move back within appropriate limits again. We have not identified how to capitalize on this effect.

The discretized representation of seismic wavefields and wavefield continuation operators requires a strategy to eliminate contamination from aliasing. Fourier sampling theory allows for the development of the rigorous Nyquist limits for arbitrary sampling of data and image axes. Using these requirements to restrict the discretized wavefield continuation process, we present criteria for determining appropriate image space Nyquist limits for arbitrary sampling choices.

As an example, we show a simple numerical case where aliased energy is introduced into the image space during migration after subsampling the shot axis. We then present three ways in which operator aliasing problems may be resolved in shot-profile migration strategies, and discuss the implications of operator aliasing on source-receiver migration formulations. Finally, an Appendix is included to provide, a rigorous development of the appropriate energy wavenumber limits as a function of data axes sampling, the extension of that development to explain the equivalence of shot-profile migration and source-receiver migration, and the introduction of imaging condition aliasing in the source-receiver migration algorithm.

This analysis has several important ramifications. Shot axis subsampling is a common practice before migration of large data sets to save time or cost. Narrow azimuth acquisition strategies, common to marine surveys, have inherent trade-offs between strike and dip resolution that are sometimes difficult to quantify. Wide azimuth land surveys are also often constrained by unequal in-line and cross-line sampling. Migrations of ocean bottom cable data also suffer from this problem due to their acquisition idiosyncrasies (though the reciprocal of our example presented later). Thus for any situation, be it acquisition design or processing choices, where one is forced to migrate data without equal numbers of shots and receivers at the same locations in both surface directions, the aliasing criteria explained herein can easily be implemented in standard wavefield continuation migration programs to enhance the quality of the image.

AXES AND ALLIES

The standard seismic acquisition grid is presented in panel (a) of Figure 1. Ease of drafting and understanding conventionally has lead geophysicists to draw these axes 90^o to each other. However, there is no reason to do so. Further, imposing the intuition that these axes are mathematically orthogonal leads to difficulties in interpreting Fourier sampling criteria that we aim to investigate here. These axes inhabit the same physical space along a 2D seismic acquisition line. Plotting them orthogonally casts an inappropriate feeling of a second physical dimension. At the limit of this argument, we contend that it is much easier to de-couple

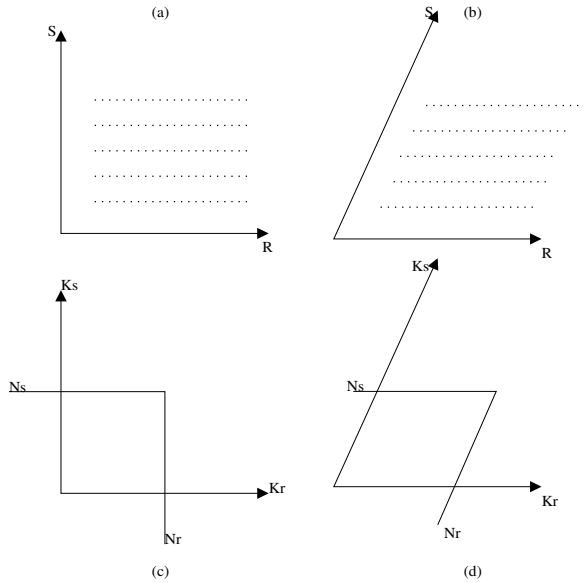

Figure 1: (a) The standard representation of the seismic acquisition grid. (b) Viable alternative to conventional orthogonal drawings. (c) Fourier transform of (a) with Nyquist sampling limits included. (d) Fourier transform of (b) with Nyquist sampling limits included. brad1-nybox [NR]

completely the origins of these axis and plot them parallel to each other. Having performed a Fourier transform across space of both the source and receiver axes, we present them in Figure 2. Viewing these three distinct axes separately aids in the interpretation of this entire argument. Unfortunately, there is an historic tendency when analyzing the acquisition grid coordinates to include midpoint-offset, mh, axes as diagonal axes to those shown in Figure 1. We will avoid the use of midpoint while casting this presentation largely in the terms of shot-profile migration, as well as explain later the development of our x-axis during the imaging condition. Further, when they are superposed, an incorrect stretching is implied. We will briefly consider the mid-point axis, in order to highlight the danger of this practice.

The mapping transformation of energy from one coordinate frame to the other has been historically defined as:

$$m = \frac{s+r}{2} \tag{1}$$

$$h = \frac{s-r}{2}\,. \tag{2}$$

The Jacobian of this system is thus,

$$J^2 = \begin{pmatrix} \frac{\partial m}{\partial r} & \frac{\partial m}{\partial r} \\ \frac{\partial m}{\partial s} & \frac{\partial m}{\partial s} \end{pmatrix} = \begin{pmatrix} \frac{1}{2} & -\frac{1}{2} \\ \frac{1}{2} & \frac{1}{2} \end{pmatrix}, \tag{3}$$

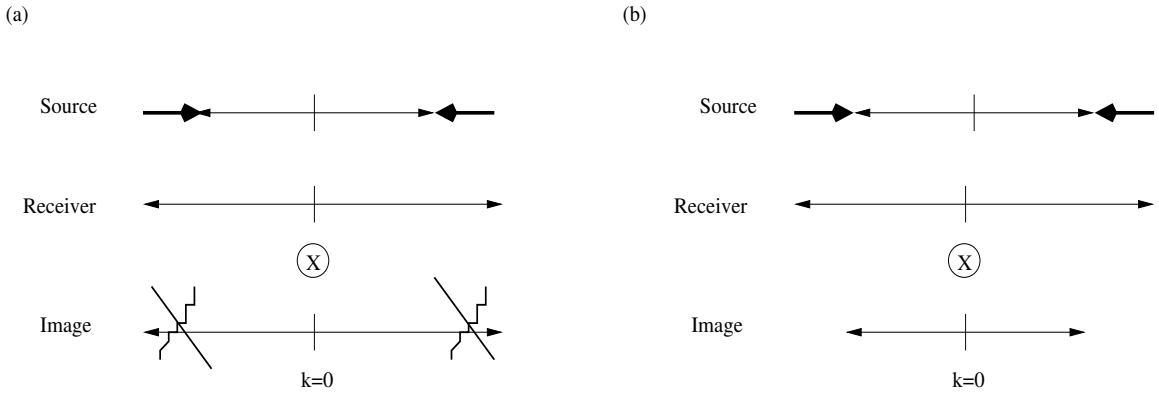

Figure 2: Lengths of the source, receiver and image axes in the Fourier domain. The circle with an x indicates the multiplication of the data axes to produce the image surface location axis during the imaging condition. Aliased replications from the source axis are represented by the bold lines pointing toward the origin. (a) If the image spaced is sampled as finely as the receiver axis, alias contamination will enter into the image. (b) Aliased contamination from the subsampled source axes is avoided when the two fields are compared during the imaging condition. brad1-waveline [NR]

which makes the determinant $1/\sqrt{2}$. Drawing a midpoint axis along the 45^o line of the sr-axis is confusing when someone attempts to find value of a particular midpoint location on the plane. Some measurement of distance must be employed as a zero-offset location does not lie on one of the original axes. The next problem we then face is which of the multitude of distance measures we should select: $l_?$. The historic choice has been the square-root of the sum of the squares: l_2. If we make that choice, we then apply the determinant presented above to cancel the $\sqrt{(2)}$ factor associated with the norm that so naturally lends itself to pieces of paper. We could have chosen any norm. Each of them would return a different number, and none of them have any more or less value for locating a seismic image on the surface of the earth.

The cross-correlation imaging condition with subsurface offset (Rickett and Sava, 2001)

$$I(x,h,z) = \sum_s \sum_\omega R(x = r-h,z,\omega)S^*(x = s+h,z,\omega), \tag{4}$$

combines the two independently propagated wavefields, *S*ource and *R*eceiver ,and generates the surface location axis x with the relationship within the arguments of the two wavefields. Note that these relations are equations for a line where both the source coordinate, s, and receiver coordinate, r, coexist. Here we see the distinction between the surface location coordinate x and midpoint. The x-axis fallows directly from the mathematics of migration. With the multiplication (across space) associated with the correlation (along time) of equation (4), the cartoons in Figure 2 should be recalled.

The Appendix develops in rigorous detail the wavenumber limits acceptable in the image to eliminate completely alias contamination. The analysis of the problem centers around the effects of the migration process on the data *grid*, without needing to consider the values of

the data on each grid node. We thus draw an analogy to the body of work available from crystallography, where structure can be analyzed mathematically without need to know what atom resides at any particular location. Thankfully, the regular Cartesian grid on which we normally acquire and process seismic data is a simple rectilinear crystal, though of several more dimensions than seen under a microscope.

The reference crystal we will consider will be the archetypal seismic grid where sources and receivers occupy all locations and share the same spacing increment. The suspicious or simply inquisitive reader can now turn to the appendix to work through the details of the following result. The maximum allowable wavenumbers, B_{x_ξ}, to avoid artifacts due to migration operator aliasing is

$$B_{x_\xi} = \frac{1}{\text{lcf}(2a_1\Delta r_\xi, 2a_2\Delta s_\xi)} = \text{lcf}(\frac{N_{r_\xi}}{a_1}, \frac{N_{s_\xi}}{a_2}) = \min(B_{r_\xi}, B_{s_\xi}) \tag{5}$$

where N_{r_ξ} and N_{s_ξ} are the Nyquist frequencies defined by fundamental sampling intervals $\Delta r_\xi = \Delta s_\xi$, a's are subsampling factors, and lcf stands for least common factor (which will change to min if the subsampling factors are integers. The subscript ξ denotes the sampling associated with the model space and is included to maintain parallelism with the appendix.

We consider three approaches to remove the aliasing problems associated with the acquisition and subsampling situations mentioned above during shot-profile migration. First, wavenumbers from the source and receiver wavefields at each depth level are band-limited to prevent the entry of aliased duplications into the image during the imaging condition. This does not require eliminating these components from the propagating wavefields, as we can save appropriate portions of the wavefields in temporary buffers for imaging condition evaluation. Second, a band-limited source function, with a wavenumber spectrum limited to the cutoff frequencies imposed by the resampled shot axis, is propagated throughout the migration process. This effectively zeros energy in the aliased band during the convolution in the imaging condition. No additional computational overhead is required for the latter alternative, though anti-aliasing by band-limited imaging requires two additional Fourier transforms for a split-step Fourier migration strategy. It should be noted, however, that both of these approaches will remove energy across both k_x and k_h axes.

A third alternative is to restrict the wavenumbers of the subsurface offset axis k_h during imaging. Casting the imaging condition in terms of it Fourier dual can allow similar mitigation options. Because $k_s - k_r = k_h$, we can select (k_s, k_r) combinations during the imaging condition that do not exceed our prescribed bandwidth. The multiplication of the source and receiver wavefields shown above takes the form of a convolution in the Fourier domain, which can be utilized to insert our anti-aliasing criteria. Lastly, decimating the receiver wavefield to match the shot increment, will be discussed in more detail with reference to shot-geophone style migration.

FLAT EARTH SYNTHETIC

A synthetic data set was generated to test the first two methods of preventing aliasing. Shot-gathers were modeled over a $2000m/s$ earth model with one flat reflector at $1000m$. Nominal shot, Δs, and receiver, Δr, spacing is $10m$. Dominant frequency of the wavelet is $30Hz$. Migration experiments were performed using both shot-profile and source-receiver algorithms. The analysis and conclusions are valid for both shot-geophone and shot-profile migrations due to their mathematical equivalence (Biondi, 2003; Shan and Zhang, 2003). However, in practice there are subtle differences between the two that will be discussed later.

The data so generated has been imaged with a split-step Fourier wave equation continuation migration kernel. The same continuation operator has been implemented in both shot-profile and source-receiver formulations. The complex valued image at the depth of the reflector was extracted without the normal summation of the frequency axis to aid in interpretation. Fourier transforms of the surface location and subsurface offset axes were then applied. Both migration strategies were used to examine several cases of data completeness. For the shot-profile migration example, four cases were considered: 1) shots at every receiver location, 2) shots at every tenth receiver location, 3) shots at every tenth receiver location imaged with a band-limited source function, and 4) shots at every tenth receiver location imaged with the selective energy imaging condition. For the source-receiver example, three cases were considered: 1) migration of all CMP's, 2) migration of CMP's from shot placements every tenth receiver location, and 3) migration of subsampled data appropriately filled with zero-traces to regain the size of the original data set. Despite the large decimation of the data for these experiments, care was taken to assure that the data were still appropriately sampled after decimation to assure that the conclusions drawn from these results are not due to acquisition aliasing.

Shot-Profile Migration

The introduction of aliasing artifacts is demonstrated by comparing panels `a` and `b` in Figure 3. Both images were constructed with the shot-profile migration algorithm using a single trace source function. Each panel shows the Fourier transformed image surface location and subsurface offset axes, (k_x, k_h, ω). In this manner the spatial energy components of the image from a particular depth in the model can be viewed. These figures capture the model space at the depth of a perfectly imaged flat reflector. Migrating shot-profiles at every receiver location as in panel `a`, shows marked difference to the wavenumber components that make up the image produced by migrating shots at every tenth shot in panel `b`. As the $k_x = 0$ aliased energy moves into the image from the replicated Fourier spectra, bands of aliased energy appear at multiples of $10m^{-1}$ on the k_x axis.

Panel `c`, also produced using every tenth shot, illustrates the effectiveness of the first two methods in eliminating the aliased energy introduced by subsampling the shot axis. The image does not suffer from aliased energy due to the use of a spatially band-limited source function with some width in space rather than a single trace. Notice also the diminished k_h bandwidth as a result of restricting energy content of the migration.

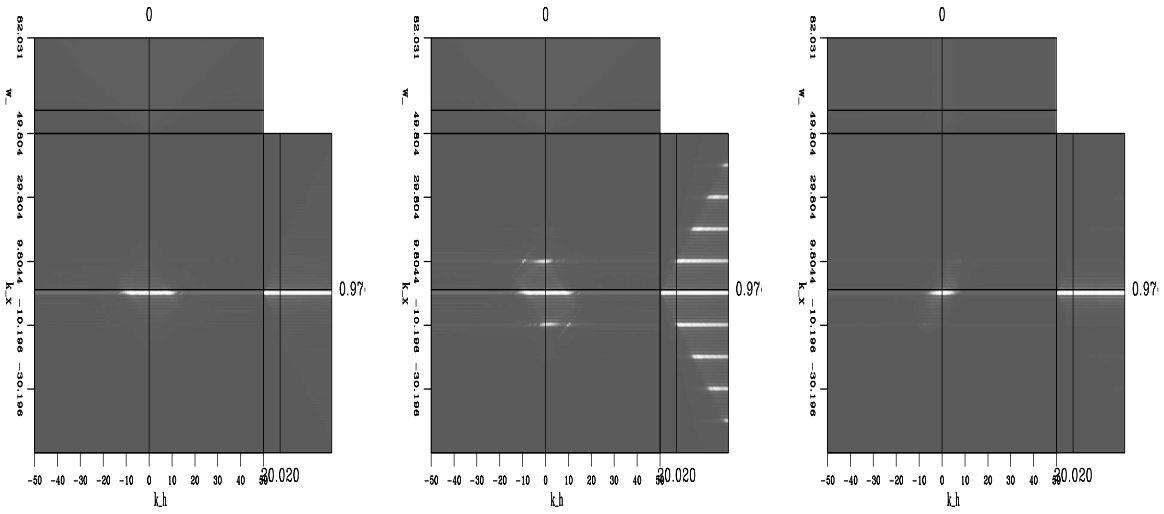

Figure 3: Panels showing image wavenumbers from migrations of different selections of available shots from the data set. Left panel was created by migrating all available shots, while the center and right panels include only every tenth shot. Note the replication of the flat reflector every $10m^{-1}$ in the center panel. The right panel is the result of restricting the migrated energy with a fat source function. Notice that the length of the reflector energy along the $k_x = 0$ axis has been limited from $10m^{-1}$ to $5m^{-1}$ indicating an imposed restriction on the number of offsets contributing to the image at any given dip. Selective energy imaging yields an identical result to the band-limited wavelet result. brad1-sp [CR]

Selective energy imaging, our second proposed method, uses band-limited versions of the source and receiver wavefields for the imaging condition. The resultant image is identical to the right panel and is accordingly not shown.

Source-Receiver Migration

Figure 4 shows analogous plots to those presented in the previous discussion. The same earth model and analysis strategy is employed for these experiments, though a source-receiver geometry for the data is employed requiring sorting the data to midpoint-offset coordinates. The same migration split-step Fourier migration kernel is used. While the panel `a` result employs a fully populated, regular data set, the others only used shots every 10 receiver locations. Panel `b` was simply sorted and migrated. Panel `c` used the same amount of live data traces as panel `b`, with zero traces replacing nine out of ten traces from the full data volume. Thus, the first and last experiments migrated the same size data cube, while second and last experiments contain the same amount of non-trivial data though they are an order of magnitude different in size.

Importantly, the second panel does not show the aliasing problems present in the second panel of Figure 3 despite the same level of shot decimation. In this experiment, the subsampling of the shot-axis is partially mapped into both of the two new coordinate axes before migration. The coordinate transform of equation (1) thus distributes the axis' lower Nyquist

limit equally to the new coordinates prior to migration. Since the output image coordinates inherit this same sampling, the resampled data naturally adhere to the band-limiting criterion of equation (5).

The image location and subsurface offset variables of these migrations have the same meaning as those discussed in the shot-profile section previously (Biondi, 2003). There have been two important modifications however due to the initial coordinate transform. First, notice the range of wavenumbers included in the second image space is drastically limited from the panel to the left showing the migration of all available shots. The resorting has effectively band-limited the image space honoring the Nyquist requirement appropriate for the image given the shot axis subsampling. Thus, the algebraic combination of source and receiver coordinates in the numerator makes this an inherently band-limited propagation method. Second, the division by two of both new axes stretches their Fourier dual domains. Notice that the alias replications in the right panel of Figure 4 appear at a wavenumber of 20 rather than the 10 seen in the shot-profile migration example. Despite the fact that the same number and sampling interval for the shot axis was used in both experiments, the division associated with the coordinate mapping has decreased the sampling interval in the space domain and stretched energy along the Fourier domain. This has happened independently of the three modes of aliasing described above and needs undoing separately as well.

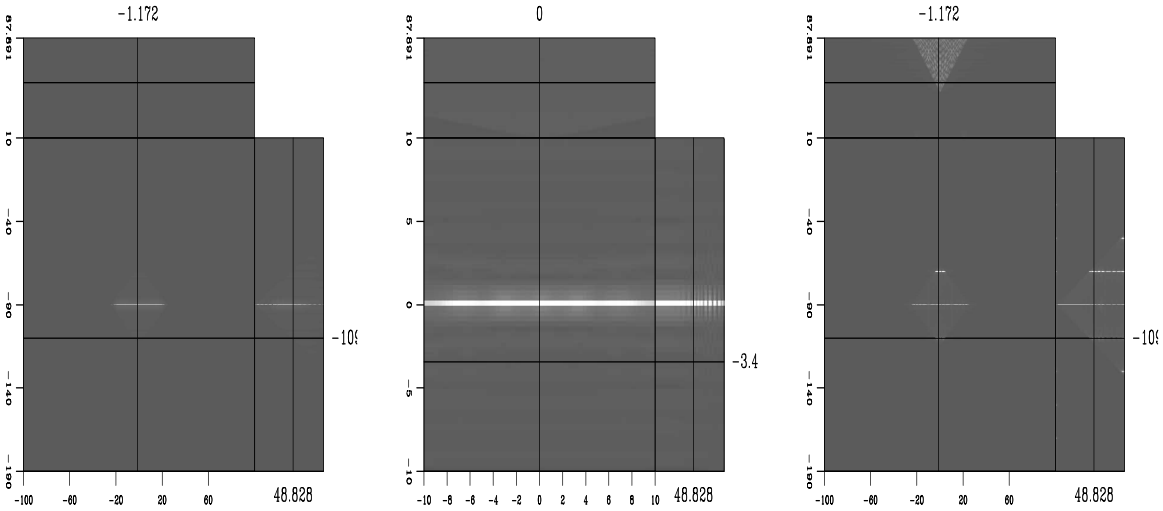

Figure 4: Source-receiver migration results. Left panel imaged with all data. Center panel imaged with every tenth shot and sorted to midpoint-offset coordinates. Right panel has zero traces inserted to fill out the decimated data set migrated in the center panel to the data set's original size. brad1-sg [NR]

Discussion

The analytical band-limit of equation (5) is the necessary criteria to appropriately delimit non-aliased wavenumbers for either wavefield continuation migration method. The amount of compression of a data axis in the Fourier domain by removing samples from the space domain

dictates the areal extent of the source function or the wavenumber limit for the limited energy imaging strategy. This problem will manifest itself primarily with shot-profile migration strategies. This is due to the fact that two conflicting sampling schemes are simultaneously available. Choosing the finer sampling for migration, results in an aliased image. Choosing the coarser sampling for the migration throws away valuable information. We have shown two methods thus far to eliminate aliased contributions to the image based on equation (A-20). We feel that it is more appropriate to use selective energy imaging conditions rather than a fat source function or band-limited continuation steps while propagating on the finest available data grid.

In practice, lateral velocity variation will cause individual wavenumber energy constituents to move about the fk-plane. At some continuation step, energy could move back and forth across the prescribed image space band-limit, and yet still be appropriate for that individual profile propagation. To allow for any beneficence from this movement, it would be unwise to either: a) propagate a band-limited source function, or b) to eliminate energy from the source and receiver wavefields during propagation steps (by either coarse resampling, or band-limiting the propagation wavefields). Therefore we recommend migrating individual shots on the fine grid, and accounting for operator aliasing in the imaging step at a modest cost increase. The output resolution will still be at least as good as a source-geophone migration.

COMPLEX EARTH EXPERIMENTS

Despite the success in removing alias artifacts with the above two methodologies, use of the bandlimited source function or the bandlimited imaging condition in areas of complex geology has one substantial limitation. Both strategies bandpass the wavefields at some point during the migration which effectively introduces focusing of the source illumination beam that propagates through the model. This is due to elimination of k_x energy in the process. Figure 5 illustrates this effect using a shot modeled over the Marmousi data set. The left panel shows an image generated from the single shot with no restrictions imposed during migration. The right panel however used the spatially bandpassed source function. The introduction of low spatial frequencies into the initial condition of the source wavefield effectively changes the impulse into a short planewave. While this is appropriate to limit aliasing when all the shots are summed, the focusing of the beam directly down is inappropriate. To limit the dip-spectrum of the geology appropriate to our sampling thereof, we have limited the directionality of the source wavefield to near vertical as well.

Instead, our last methodology attempts to include all propagation directions by choosing portions of the wavenumber spectrum of the receiver wavefield that are appropriately limited for each component of the source wavefield (or vice-versa). While the goal of the imaging condition is a cross-correlation of the two wavefields followed by extraction of the zero time-lag as shown in equation (4), the process in effect multiplies across the space axis. Further, to calculate offset, a spatial cross-correlation without summation is employed. The Fourier dual of these two implicit operations are convolution and multiplication respectively. Thus, by transforming our wavefields into the wavenumber domain, the imaging condition takes the

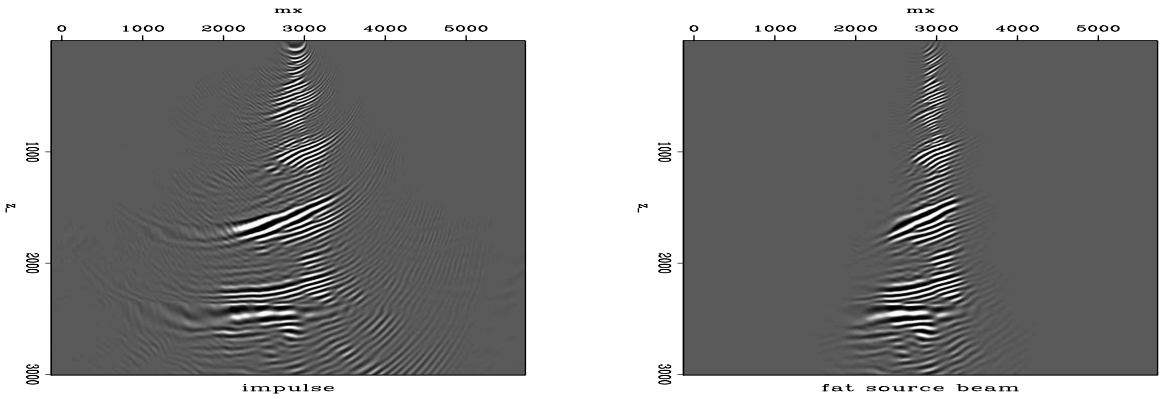

Figure 5: Left: Image from a single shot of the Marmousi data conventionally migrated and with anti-aliasing limits. The limited propagation angles are inappropriate. Center: Full bandwidth shot image. Right: Dip-limited image via partial convolution imaging condition. brad1-marm [NR]

form of the convolution

$$I(x;h)|_z,\omega = R(x-h)S^*(x+h)I(k_x;h)|_z,\omega = \sum_\omega \sum_j \tilde{R}(k_x = k_r - j,z,\omega)\tilde{S}^*(k_s = j,z,\omega)e^{-ijh}. \quad (6)$$

Inspecting the above, we notice that the counting subscript j is actually the wavenumber offset axis with with the exponential inverse Fourier transforming the axis during summation to give a single offset panel. Thus, by not summing this dimension, we build the Fourier transform of the offset axis.

Using this formulation, and the fact that $k_r - k_s = k_h$, we can bandlimit the image space by only allowing offset wavenumber combinations where $k_r - k_s$ is less than the prescribed bandlimit. Thus, while calculating k_x wavenumbers for the image space, only a limited and varying band from the offset axis is considered. In this manner, we can limit reflectors to different offset spectra depending on their structural dip. Figure (6) shows the result of this implementation. Several features are prominent. First, the thick, fast layer at $(3000m, 2500m)$ contains dipping energy that is not in the impulse response. This is a dip ringing due to implementing a hard cutoff in the Fourier domain when selecting wavenumbers for imaging. This noise should cancel during summation of many shots. Unfortunately, the convolutional imaging condition has Fourier domain periodicity problems that are well avoided by operating in the space domain. Further, there did not seem to be significant improvement over illumination angle as compared to the two previous methods proposed. Finally, given that our effective range of sub-surface offset is actually quite limited, the huge cost differential, $O(n_x n_h)$ vs. $O(n_x^2)$, makes the decision for us.

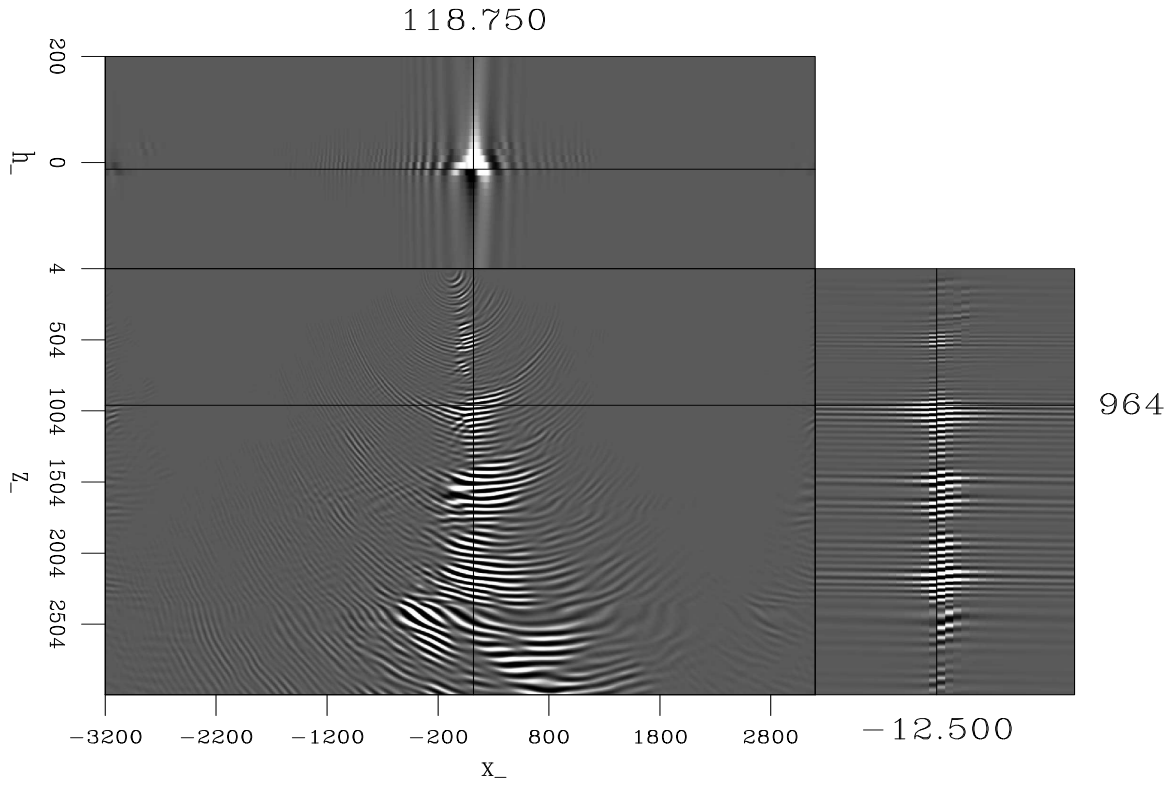

Figure 6: Single shot image from the band-limited convolutional imaging condition. The wave-number bandwidth was limited to 1/8 of the receiver Nyquist limit. brad1-off-cube [NR]

CONCLUSIONS

We conclude that operator aliasing artifacts are indeed introduced during prestack wavefield continuation migration when s- or r-axes are allowed to deviate from a regular grid. This problem is thus manifest both when we choose to subsample the number of shots available from the data or design a survey without shots at every receiver location (or in reciprocal cases like OBC surveys).

Source-receiver migration strategies conveniently side-step the bulk of the operator aliasing problem by effectively performing all propagation and imaging on the coarsest available grid. Thus during every wavefield continuation step, we are only propagating energy that lies below the Nyquist wavenumber for the final image space. However, this constraint can be much too stringent when compared to the sampling criteria set out, and presumably met, during the acquisition effort. This migration style will propagate energy along fewer traces than shot-profile methodologies, although it lacks some ability to control the quality of the image. The fact that the model output of source-receiver migration is on a twice finer grid than acquisition or the model produced with shot-profile migration does not exclude this migration strategy from the imaging condition aliasing described by Zhang et al. (2003). The division in the mapping of equation (1) is responsible for this, but does not perform the necessary

interpolation to avoid imaging condition aliasing. Performing the imaging condition in the Fourier domain does not entail additional cost for this split-step Fourier migration kernel, and conveniently eliminates the need to interpolate the wavefields by a factor of two to address the aliasing due to multiplication as the output of the convolution is inherently twice the size of the two inputs.

Given some knowledge of the dip content of the data, it is possible to extend the boundaries of the rigorous anti-aliasing criteria presented. Using both positive and negative one-sided band-limits can include high wavenumber energy that can improve the image in areas of steep dips and the shallow section of the model. Therefore, when challenged with imaging important steeply dipping targets, decisions concerning acquisition design or the level of decimation along different directions for migration can be made with a better understanding of the consequences to the final product. Finally, it has been noticed that the rigorous Nyquist limits are substantially too restrictive in practice with real data. In reality, the benefits of some level of anti-aliasing are realized when inspecting the dipping canyon features of the Marmousi data, though the limitation imposed during the imaging condition was much more relaxed than indicated by the theory and needed to be found through experimentation.

Further, if a subsample of a data set is imaged with a shot profile migration strategy, full bandwidth source and receiver wavefields, $W_s(\mathbf{x}, z, \omega)$ and $W_r(\mathbf{x}, z, \omega)$, could be saved for future migration efforts. An imaging condition with the appropriate band-limitation across the spatial axes can be applied with partial or complete sets of these migrated volumes. Thus incremental increases in image quality can be achieved while avoiding re-migration of data by augmenting a library of wavefields (if adequate storage capacity is available).

REFERENCES

Biondi, B., 2003, Equivalence of source-receiver migration and shot-profile migration: Geophysics, accepted for publication.

Claerbout, J. F., 1971, Toward a unified theory of reflector mapping: Geophysics, **36**, no. 03, 467–481.

Rickett, J., and Sava, P., 2001, Offset and angle domain common-image gathers for shot-profile migration: SEP–**108**, 27–34.

Shan, G., and Zhang, G., 2003, Equivalence between shot-profile and source-receiver migration: SEP–**113**, 121–126.

Zhang, Y., Sun, J., and Gray, S., 2003, Aliasing in wavefield extrapolation prestack migration: Geophysics, **68**, no. 2, 629–633.

APPENDIX A

Surface seismic acquisition involves the acquisition of a set of discrete wavefield measurements using sources and receivers that populate a 2D recording surface. In wave equation migration, the wavefield continuation component of the experiment involves a downward extrapolation of the recorded wavefield from the acquisition surface to subsurface layers within an earth model. Finally, the imaging component requires the extraction of energy from the wavefield by the evaluation of an imaging condition (Claerbout, 1971). Central to these three procedures is the geometry on which the experiment and accompanying processing are based. From a practical processing viewpoint, the ideal data set would be defined on a uniformly-sampled 3D (for 2D surveys) or 5D (for 3D surveys) acquisition grid. This Appendix seeks to analyze the data grid through all of the afore-mentioned steps as if studying the structure of a crystal.

To address the issue of aliasing, Fourier sampling theory will be applied. This theory provides the necessary and sufficient conditions for preserving the information content of a continuous physical wavefield represented in a discrete manner. One important tenet of sampling theory is that the highest frequency recoverable from a regularly-sampled data set is independent of values at sample locations, but dependent on the interval between neighboring samples. Aliasing considerations for seismic wavefields are likewise dependent on the spacing between individual points in the lattice. In light of the above, we will dissociate the acquisition geometry of a seismic experiment from the values recorded at the acquisition points, and represent the former with a multi-dimensional Shah function. Using this representation, the effects on the lattice structure of the processes of downward continuation and imaging condition evaluation are readily examined.

Throughout this presentation, we will maintain the formulation of the seismic experiment in the shot-geophone coordinate system. Shan and Zhang (2003) points out that a correlation of the source and receiver wavefields is implied in this migration formulation. This observation introduces a convolution of source and receiver lattices. A lattice convolution, whether in a shot-geophone or shot-profile migration setting, gives rise to the phenomenon of image condition aliasing (Zhang et al., 2003). This phenomenon arises when two wavefields multiplicatively interfere to yield an aliased Moiré pattern with frequencies up to twice those of the original wavefields. To account for this phenomenon we will assume that the wavefield is already interpolated by a factor of two, and that the lattice upon which this discussion begins is not the acquisition grid, but is of twice finer spacing. Finally, although the theory as developed below is strictly for 2D seismic experiments, the extension to 3D is a trivial matter and is omitted for clarity.

Lattice basis of seismic wavefields

We choose to represent a seismic wavefield, W, by dissociating the underlying interpolated acquisition lattice (IAL), $\mathcal{L}$, from the discretely sampled values of the continuous wavefield, f^W. Lattice $\mathcal{L}$ is defined over experimental source and receiver coordinates, r_ξ and s_ξ, and

time and depth coordinates, t_ξ and z_ξ. Importantly, the underlying grid function is only a construct of the experimental process and is associated, accordingly, with model space coordinates $\mathcal{L}(r_\xi, s_\xi, t_\xi, z_\xi)$. This stands in contrast to the continuous wavefield function defined by corresponding continuous variables, $f^W(r,s,t,z)$. Written in this manner, it becomes natural to associate the act of observation with the mapping from physical (continuous) to experimental (discrete) variables,

$$W(r_\xi, s_\xi, t_\xi, z_\xi) = \mathcal{L}(r_\xi, s_\xi, t_\xi, z_\xi)\, f^W(r,s,t,z)\, \delta(r_\xi - r)\, \delta(s_\xi - s)\, \delta(z_\xi - z)\, \delta(t_\xi - t). \quad \text{(A-1)}$$

Note, that we define W as the entire experimental wavefield including traces from all source and receiver pairs. This volume is separable into many different subsets, but we will keep it in tact. One way to represent lattice $\mathcal{L}$ is with a 4D infinite sum over delta functions (i.e. a 4D Shah function),

$$\mathcal{L}(r_\xi, s_\xi, t_\xi, z_\xi) = \sum_{u_r,u_s,u_t,u_z=-\infty}^{\infty} \delta(r_\xi - a_r u_r \Delta r_\xi)\delta(s_\xi - a_s u_s \Delta s_\xi)\delta(t_\xi - a_t u_t \Delta t_\xi)\delta(z_\xi - a_z u_z \Delta z_\xi). \quad \text{(A-2)}$$

In equation (A-2), variables (a_r, a_s, a_t, a_z) are subsampling factors over the fundamental discretization intervals $(\Delta r_\xi, \Delta s_\xi, \Delta t_\xi, \Delta z_\xi)$, and (u_r, u_s, u_t, u_z) are the associated summation indicies of the delta functions. It is assumed that for our ideal grid $\Delta r_\xi = \Delta s_\xi$ and any departures from this equality may be represented through the subsampling factors. Throughout the development, unless specified otherwise, the summation from $-\infty$ to ∞ in equation (A-2) is assumed. Due to the fact that no experiment is ever carried out with infinite extent, padding the wavefields to infinity with zero traces maintains the rigor of this evaluation.

Band-limited lattices

In a seismic experiment, measurements are necessarily acquired at discrete sampling intervals. This fact requires placing a restriction on the frequency content representable on the 4-D lattice. One convenient manner to do this is to apply a 4-D Rect function in the frequency domain to cut off frequencies greater than predefined values [e.g. $(B_{r_\xi}, B_{s_\xi}, B_{t_\xi}, B_{z_\xi})$]. To accomplish this, equation (A-2) is first Fourier transformed over all variables to yield,

$$\mathcal{L}(k_{r_\xi}, k_{s_\xi}, \omega_\xi, k_{z_\xi}) = \sum_{u_1,u_2,u_3,u_4} \delta(k_{r_\xi} - \frac{u_1}{a_1 \Delta r_\xi})\delta(k_{s_\xi} - \frac{u_2}{a_2 \Delta s_\xi})\delta(\omega - \frac{u_3}{a_3 \Delta t_\xi})\delta(k_{z_\xi} - \frac{u_4}{a_4 \Delta z_\xi}). \quad \text{(A-3)}$$

A 4D Rect function, Π, with arguments (in 1D)

$$\Pi(B_{r_\xi}) = \begin{cases} 1 & \text{for } |r_\xi| < \frac{1}{2B_{r_\xi}} \\ 0 & \text{for } |r_\xi| \geq \frac{1}{2B_{r_\xi}} \end{cases},$$

is then applied to the infinite Fourier domain lattice $\mathcal{L}$ to yield a band-limited version $\mathcal{L}_{FL}$,

$$\mathcal{L}_{FL}(k_{r_\xi}, k_{s_\xi}, \omega, k_{z_\xi}) = \mathcal{L}(k_{r_\xi}, k_{s_\xi}, \omega, k_{z_\xi})\Pi(B_{r_\xi} k_{r_\xi}, B_{s_\xi} k_{s_\xi}, B_{t_\xi}\omega, B_{z_\xi} k_{z_\xi}). \quad \text{(A-4)}$$

Applying an inverse Fourier transform over all 4 dimensions to lattice $\mathcal{L}_{FL}$ yields,

$$\mathcal{L}_{FL}(r_\xi, s_\xi, t_\xi, z_\xi) = \mathcal{L}(r_\xi, s_\xi, t_\xi, z_\xi) *_{r_\xi} *_{s_\xi} *_{t_\xi} *_{z_\xi} FL(r_\xi, s_\xi, t_\xi, z_\xi), \tag{A-5}$$

where

$$FL(r_\xi, s_\xi, t_\xi, z_\xi) = \frac{\text{sinc}(\frac{r_\xi}{B_{r_\xi}}, \frac{s_\xi}{B_{s_\xi}}, \frac{t}{B_{t_\xi}}, \frac{z_\xi}{B_{z_\xi}})}{B_{r_\xi} B_{s_\xi} B_{t_\xi} B_{z_\xi}}, \tag{A-6}$$

and the subscripts on the convolution symbol, $*$, delimit the coordinate over which the convolution is applied. Thus the seismic wavefield may be represented by,

$$W(r_\xi, s_\xi, t_\xi, z_\xi) = \mathcal{L}_{FL}(r_\xi, s_\xi, t_\xi, z_\xi)\, \delta(z_\xi) f^W(r_\xi, s_\xi, t_\xi, z_\xi). \tag{A-7}$$

It is important to emphasize that the lattice $\mathcal{L}_{FL}$ in equation (A-7) represents only the lattice structure on which the data wavefield is overlaid. For individual seismic experiments, the values at each location will vary, while the lattice structure remains invariant. Utilizing the crystal structure analogy again, any atom may inhabit a node in the lattice, but there must be one and only one atom present.

Downward continuation with the DSR

In this section we apply the double square root (DSR) operator to extrapolate the recorded wavefield of equation (A-7) through the depth coordinate of the lattice. After initially Fourier transforming the wavefield into k_{r_ξ}, k_{s_ξ}, and ω_ξ, the first application of the DSR yields a new wavefield at depth step $z_\xi = a_4 \Delta z_\xi$. Mathematically, this is represented by:

$$\begin{aligned} W(k_{r_\xi}, k_{s_\xi}, \omega, z_\xi) = & \quad \delta(z_\xi - a_z \Delta z_\xi) *_{z_\xi} \left[DSR(k_{r_\xi}, k_{s_\xi}, \omega, z_\xi) W(k_{r_\xi}, k_{s_\xi}, \omega, z_\xi = 0) \right] \\ = & \quad \delta(z_\xi - a_z \Delta z_\xi) *_{z_\xi} \left[DSR(k_{r_\xi}, k_{s_\xi}, \omega, z_\xi) f^W \mathcal{L}_{FL}(k_{r_\xi}, k_{s_\xi}, \omega, z_\xi) \delta(z_\xi) \right] \\ = & \quad \left[DSR(k_{r_\xi}, k_{s_\xi}, \omega, z_\xi) f^W \right] \mathcal{L}_{FL}(k_{r_\xi}, k_{s_\xi}, \omega, z_\xi + a_z \Delta z_\xi) \delta(z_\xi - a_z \Delta z_\xi). \end{aligned} \tag{A-8}$$

The periodicity of the lattice over depth coordinate z_ξ enables the Shah function index u_z to be shifted by $a_z \Delta z_\xi$ such that equation (A-8) reads,

$$W(k_{r_\xi}, k_{s_\xi}, \omega, z_\xi) = \left[DSR(k_{r_\xi}, k_{s_\xi}, \omega, z_\xi) f^W \right] \mathcal{L}_{FL}(k_{r_\xi}, k_{s_\xi}, \omega, z_\xi) \delta(z_\xi - a_4 \Delta z_\xi)\,. \tag{A-9}$$

By extension, any continuation step operating on a wavefield will take the same form. Applying an inverse Fourier transform over coordinates k_{r_ξ} and k_{s_ξ} yields,

$$W(r_\xi, s_\xi, \omega, z_\xi = a_4 \Delta z_\xi) = H(r_\xi, s_\xi, \omega, z_\xi) *_{r_\xi} *_{s_\xi} \left[\mathcal{L}_{FL}(r_\xi, s_\xi, \omega, z_\xi) \delta(z_\xi - a_4 \Delta z_\xi) \right] \tag{A-10}$$

where , for convenience, H is defined by,

$$H(r_\xi, s_\xi, \omega, z_\xi) = \mathcal{F}^{-1}_{k_{r_\xi}, k_{s_\xi}} \left[DSR(k_{r_\xi}, k_{s_\xi}, \omega, z_\xi) f^W \right], \tag{A-11}$$

where $\mathcal{F}$ is the Fourier transform operator. It is important to note here that the convolution of lattice $\mathcal{L}_{FL}$ with filter H does not change the location of the sample points. Rather, it operates only on the amplitudes at the predefined locations.

Evaluation of imaging condition

While we have maintained our coordinate system thus far in parallel with a shot-receiver migration strategy, we will now detail the evaluation of the imaging condition with the order of operations normally associated with shot-profile migration. In fact, the convolution of the source and receiver grids associated with the imaging condition (and gives rise to imaging condition aliasing) can be performed/implied before the migration which is common to resorted mh-coordinate migrations or at each depth step within the migration. As we have maintained the distinctiveness of the source and receiver grids to this point, the convolution of their axes must now be evaluated.

Calculating Common Image Gather (CIG) offsets involves the evaluation of an imaging condition at all acceptable values of r_ξ and s_ξ. This gives rise to two new image space variables: the horizontal image coordinate for the earth model, x_ξ, and the subsurface horizontal offset coordinate, h_ξ. These variables have much similarity to the data space variables midpoint and offset. In a strictly $v(z)$ medium, these axes overlay. However, in more complicated media, the midpoint variable is somewhat misleading. This is because the wavefield continuation extrapolates energy from a midpoint on the surface to a different midpoint as the wavefields are successively downward-continued. Thus, mixing these two ideas is inappropriate. Source and receiver coordinates and horizontal and sub-surface offset coordinates are related through transforms $r_\xi = x_\xi + h_\xi$ and $s_\xi = x_\xi - h_\xi$. The new coordinate, h_ξ, a derived parameter with a magnitude equal to an integer multiple of Δx_ξ, is naturally represented as the product of an integer multiplication factor h and horizontal image space discretization interval Δx_ξ (i.e. $h_\xi = h\Delta x_\xi$) that will most commonly be unity.

Using these definitions, the image cube may be constructed by applying the general correlation imaging condition to wavefield W,

$$I(x_\xi, z_\xi, h_\xi) = \sum_\omega \Big[\delta(r_\xi - h_\xi) *_{r_\xi} W(r_\xi, s_\xi, \omega, z_\xi) *_{s_\xi} \delta(s_\xi + h_\xi)\Big] \delta(r_\xi - x_\xi)\delta(s_\xi - x_\xi) \quad \text{(A-12)}$$

Note that this expression reduces to the familiar zero subsurface offset form when $h_\xi = 0$,

$$I(x_\xi, z_\xi) = \sum_\omega W(r_\xi, s_\xi, \omega, z_\xi)\delta(r_\xi - x_\xi)\delta(s_\xi - x_\xi). \quad \text{(A-13)}$$

The convolution arguments applied to wavefield W, in equation (A-12), yield

$$\begin{aligned} I(x_\xi, z_\xi, h_\xi) = &\quad \textstyle\sum_\omega \Big[\delta(r_\xi - h\Delta x_\xi) *_{r_\xi} W(r_\xi = x_\xi, s_\xi = x_\xi, \omega, z_\xi) *_{s_\xi} \delta(s_\xi + h\Delta x_\xi)\Big] \\ = &\quad \textstyle\sum_\omega W(r_\xi - h\Delta x_\xi = x_\xi, s_\xi + h\Delta x_\xi = x_\xi, \omega, z_\xi). \end{aligned} \quad \text{(A-14)}$$

Before continuing with this development, it is useful here to stop and interpret the meaning of equations (A-12) and (A-14). The imaging condition itself builds the image-space coordinate axes x and h during the convolution expressed above. The arguments within the wavefield W of equation (A-14) are the equations of a line. This line, x_ξ, defines the axis for surface location of the image, and is independent of any assumptions about surface midpoints during the experiment. This is one reason [2]we have avoided using the midpoint variable, m. These

[2]Recall that the other is the in measuring along it.

two coordinates indeed share many traits, though the midpoint concept is an arbitrary, while intuitive and convenient, coordinate transform. Surface location, x_ξ, is a rigorous development required by the imaging process.

Continuing our derivation, we now reintroduce the lattice in equation (A-10) to the imaging condition which yields,

$$I(x_\xi, z_\xi, h_\xi) = \sum_\omega H(r_\xi, s_\xi, \omega, z_\xi) *_{r_\xi} *_{s_\xi} \mathcal{L}_{FL}(x_\xi = r_\xi - h\Delta x_\xi, x_\xi = s_\xi + h\Delta x_\xi, \omega, z_\xi) \tag{A-15}$$

However, $h\Delta x_\xi$ is an integer shift by Δx_ξ and is defined only at known points on the lattice allowing the index of the Shah function to be shifted to yield,

$$I(x_\xi, z_\xi, h_\xi) = \mathcal{L}_{FL}(r_\xi = x_\xi, s_\xi = x_\xi, z_\xi) *_{r_\xi} *_{s_\xi} \sum_\omega \mathcal{L}_{FL}(\omega) H(r_\xi, s_\xi, \omega, z_\xi) \tag{A-16}$$

Expanding lattice $\mathcal{L}_{FL}$ into its components $\mathcal{L}$ and FL,

$$I(x_\xi, z_\xi, h_\xi) =$$
$$\mathcal{L}(r_\xi = x_\xi, s_\xi = x_\xi, z_\xi) *_{r_\xi} *_{s_\xi} *_{z_\xi} FL(r_\xi = x_\xi, s_\xi = x_\xi, z_\xi) *_{r_\xi} *_{s_\xi} \sum_\omega \mathcal{L}_{FL}(\omega) H(r_\xi, s_\xi, \omega) FL(\omega)$$

and applying a Fourier transform over coordinates r_ξ, s_ξ, and z_ξ yields,

$$I(k_{x_\xi}, k_{z_\xi}, k_{h_\xi}) = \left[\mathcal{L}(k_{r_\xi} = k_{x_\xi}, k_{s_\xi} = k_{x_\xi}, k_{z_\xi}) \Pi(B_{r_\xi} k_{r_\xi} = B_{r_\xi} k_{x_\xi}, B_{s_\xi} k_{s_\xi} = B_{s_\xi} k_{x_\xi}, B_{z_\xi} k_{z_\xi})\right] G,$$
$$G(k_{r_\xi} = k_{x_\xi}, k_{s_\xi} = k_{x_\xi}, \omega) = \mathcal{F}_{r_\xi, s_\xi}\left[\sum_\omega \mathcal{L}_{FL}(\omega) H(r_\xi, s_\xi, \omega) FL(\omega)\right]. \tag{A-17}$$

The Rect functions of coordinates k_{r_ξ} and k_{s_ξ} are collapsed back to a single Rect function in k_{x_ξ}, where the frequency limit is given by $min(B_{r_\xi}, B_{s_\xi})$. The *min* function arises because the maximum grid-spacing along either shot or receiver axis alone dictates the aliasing criteria for the k_x-axis. This also allows for simplified calculations in the particular case. Generally, however, the bracketed expression in equation (A-17) is

$$\mathcal{L}(k_{r_\xi} = k_{x_\xi}, k_{s_\xi} = k_{x_\xi}, k_{z_\xi}) =$$
$$\sum_{u1, u2 = -\min(B_{r_\xi}, B_{s_\xi})}^{\min(B_{r_\xi}, B_{s_\xi})} \sum_{u_4} \delta(k_{x_\xi} - \frac{u_1}{a_1 \Delta r_\xi}) \delta(k_{x_\xi} - \frac{u_2}{a_2 \Delta s_\xi}) \delta(k_{z_\xi} - \frac{u_4}{a_4 \Delta z_\xi}). \tag{A-18}$$

The summations of the delta functions over u_1 and u_2 collapse to a single summation over the variable with the lowest common factor (lcf),

$$\mathcal{L}(k_{x_\xi}, k_{z_\xi}) = \sum_{u = -\min(B_{r_\xi}, B_{s_\xi})}^{\min(B_{r_\xi}, B_{s_\xi})} \sum_{u_4 = -d_1 \Delta z_\xi}^{d_1 \Delta z_\xi} \delta(k_{x_\xi} - \frac{u}{\mathrm{lcf}(a_1 \Delta r_\xi, a_2 \Delta s_\xi)}) \delta(k_{z_\xi} - \frac{u_4}{a_4 \Delta z_\xi}). \tag{A-19}$$

The horizontal image coordinate is being sampled at a spacing $\mathrm{lcf}(a_1\Delta r_\xi, a_2\Delta s_\xi)$. Thus, for aliasing to be absent the following condition must hold,

$$B_{x_\xi} = \min(B_{r_\xi}, B_{s_\xi}) = \frac{1}{\mathrm{lcf}(2a_1\Delta r_\xi, 2a_2\Delta s_\xi)} = \mathrm{lcf}(\frac{N_{r_\xi}}{a_1}, \frac{N_{s_\xi}}{a_2}) \tag{A-20}$$

where N_{r_ξ} and N_{s_ξ} are the Nyquist frequencies defined by fundamental sampling interval Δr_ξ and Δs_ξ. Thus, the alias-free wavefield is given by the following geometry

$$\mathcal{L}(k_{x_\xi}, k_{z_\xi}) = \sum_{u=-\min(\frac{N_{r_\xi}}{a_1}, \frac{N_{s_\xi}}{a_2})}^{\min(\frac{N_{r_\xi}}{a_1}, \frac{N_{s_\xi}}{a_2})} \sum_{u_4=-d_1\Delta z_\xi}^{d_1\Delta z_\xi} \delta(k_{x_\xi} - \frac{u}{\max(a_1\Delta r_\xi, a_2\Delta s_\xi)})\delta(k_{z_\xi} - \frac{u_4}{a_4\Delta z_\xi}). \tag{A-21}$$

Notice that for the simplified case of zero-offset migration, the pre-supposed notion that there are no operator aliasing artifacts introduced can be shown conclusively within the presentation above. Without two different sampling intervals, be they source/receiver or orthogonal surface coordinates, there are no choices for the min operator in equation (**??**) nor the max operator of equation (A-21). Instead, the sole variable available, surface location x, dictates the sampling of the model space.

Notice that for the simplified case of zero-offset migration, the pre-supposed notion that there are no operator aliasing artifacts introduced can be shown conclusively within the presentation of the above results. Without two possibly different sampling intervals, for source and receiver grids, there are no choices for the min operator in equation (A-20) nor the max operator of equation (A-21). Instead, the sole variable available, surface location, dictates the sampling of the model space. This does not however release zero-offset migrations from the ramifications of image condition aliasing, as the implied correlation of the source wavefield associated with source-receiver migrations is still present.